Comparison of the Spatial Location of Seafloor Massive Sulfide Deposits and Deep Mantle Structure Based on Geophysical Fields in the Northern Near-Equatorial Segment of the Mid-Atlantic Ridge

S. Yu. Sokolov[a], * and A. S. Bich[b]

[a] Geological Institute, Russian Academy of Sciences, Moscow, 119017 Russia
[b] Gramberg All-Russia Scientific Research Institute for Geology and Mineral Resources of the Ocean (VNIIOkeangeologia), St. Petersburg, 190121 Russia
*e-mail: sysokolov@yandex.ru

Abstract—Comparison of the geophysical data obtained along the Mid-Atlantic Ridge (MAR) segment between 10° and 25° N and seafloor massive sulfide (SMS) occurrences made it possible to reveal a number of regularities and relationships in their spatial distribution. SMSs are grouped in the areas with the following features: near-subvertical "microplumes" which a single axial anomaly of the MAR determined by the UU-P07 seismotomographic model is divided into; maxima of Bouguer anomalies between the Vema and Kane fracture zones corresponding to solid mantle volumes and minimum magmatic flow rate; pronounced alternation of spatiotemporal seismicity "voids" and "bands" with a step of ~1.5°, comparable to the near-surface δVp minima; inversion of spreading rate asymmetry from the east of the MAR to the west within 20° and 24° N south of the Kane Fracture Zone with nontransform south-oriented displacements; and areas with a positive correlation of Bouguer anomalies and the terrain between 19° and 22° N. The relationship of SMSs with the specified geophysical features forms a basis for predicting this type of seabed minerals.

INTRODUCTION

The correlation of geological and geophysical parameters along the Mid-Atlantic Ridge (MAR) (Fig. 1, item 7) with tomographic data recording a rheological status of the upper mantle is very effective as an approach for geodynamic interdisciplinary study of the structure. E. Bonatti (1996) was one of the first to apply it. Based on the structural features of the axial part of the Atlantic region compared with the seismic tomography data in the cited work, large fault zones with an active area length of more than 200 km are spatially related to "cold" blocks of the upper mantle. Bonatti proposed two possible scenarios: mantle cooling through a macrofractured environment and initial long-lived "cold" blocks, along the boundaries of which large fault zones arise. The analysis of all data reported in (Bonatti, 1996) resulted in a conclusion supporting the second scenario. This result was obtained with a seismotomographic section along the MAR according to the RG5.5 model (Zhang and Tanimoto, 1992) with 5° × 5° cell parameterization

(500 km). As a result, cold zones were detected in the equatorial segment and at latitudes of approximately ±50°. The RG5.5 model was a great achievement in terms of detail: harmonics of up to the 36th order were processed, but not to the full depth of the mantle, only up to 500 km. The detail in the MAR zone for S-wave velocity variations was supplemented by the data on phase and group velocities of surface waves to provide a qualitative leap for such models in the areas with a low seismicity and a rare seismological network. A detail of the current models of seismic velocity variations along the MAR (Sokolov et al., 2022) makes it possible to compare the deep mantle characteristics with the clusters of SMS occurrences on the surface such as sulfide mounds of seafloor massive sulfides (SMSs) studied in the course of Polar Marine Geosurvey Expedition and VNIIOkeangeologia research cruises. In addition, the data on gravity field and its transformants, heat flow, seismicity, anomalous magnetic field, spreading rates, and bottom terrain make it possible to reconstruct additional geophysical characteristics of the mantle which form the distribution
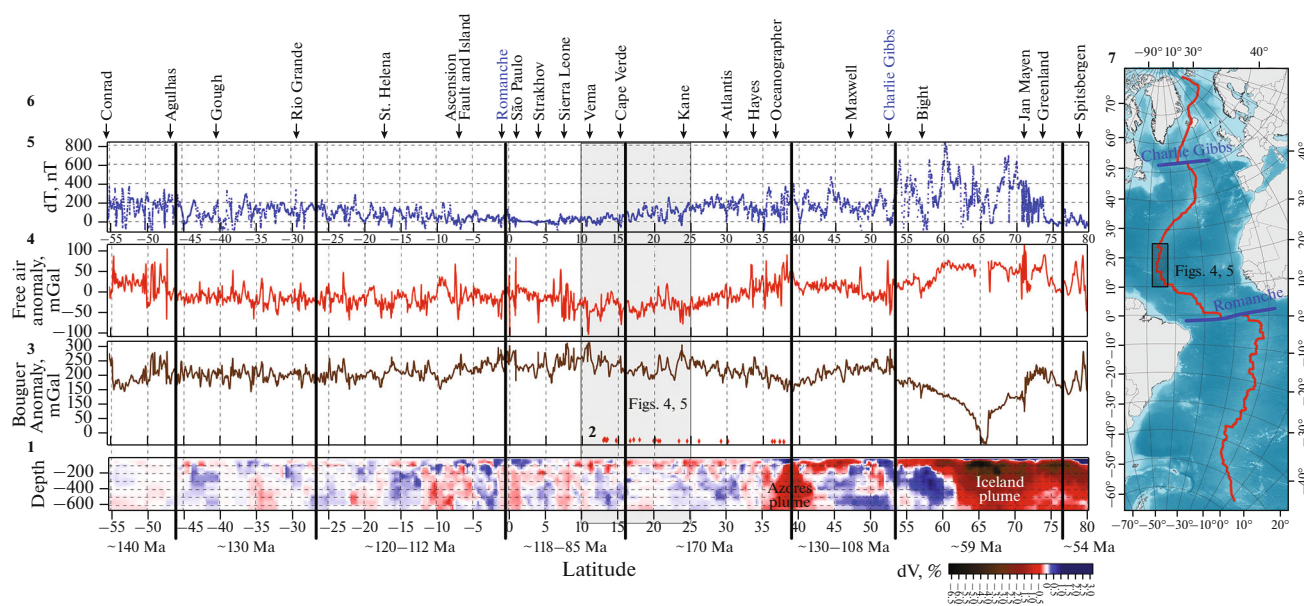
Fig. 1. Correlation of geological and geophysical parameters along MAR axis after (Sokolov, 2018) with modifications and MAR segmentation in terms of age of initiated spreading processes after (Sokolov et al., 2020). SMS-rich area is indicated by gray rectangle. (1) Variations in velocities δVp according to UU-P07 model (Amaru, 2007; Hall and Spakman, 2015; Van der Meer et al., 2018); (2) manifestations of SMS hydrothermal structures after (Beaulieu and Szafranski, 2020) and data obtained by VNIIOkeangeologia in study area; (3) Bouguer anomalies (mGal) on 5′ grid; (4) free air gravity anomalies (free air) (mGal) (Sandwell and Smith, 1997) on 5′ grid; (5) AMF along MAR axis (nT) (Maus et al., 2009) on 2′ grid; (6) intersection with MAR and names of major transform faults; (7) map of Atlantic region with MAR position in profile (red line); Romanche and Charlie Gibbs demarcation faults (blue lines) and SMS-rich area (black rectangle) whose geological and geophysical parameters are given in Figs. 4 and 5.

trends of SMS deposits. These trends are studied in this work.

CORRELATION OF GEOPHYSICAL DATA ALONG THE MAR AND THEIR SPECIFIC FEATURES IN THE NORTHERN EQUATORIAL SEGMENT OF THE MAR

The newly developed, more detailed models are based on teleseismic data with a spatial resolution of ~100 km in seismic zones and supplement understanding of the along-axis tomographic anomaly under the MAR. The UU-P07 model (Amaru, 2007; Hall and Spakman, 2015; Van der Meer et al., 2018) was used in this paper. It is distinguished by a 3D initial approximation of the velocity model, starting from which the arrival time residuals of seismic events at recording stations are calculated and minimized. For a long time, the radially symmetric PREM (Preliminary Reference Earth Model) was chosen as the initial approximation by the model creators (Su and Dziewonski, 1997). However, by the end of the 2000s, almost all calculated models based on low-frequency spherical harmonics of up to $l = 20$ ceased to be different (Becker and Boschi, 2002). As a result, 3D initial approximations were put into practice (Amaru, 2007), and the quality of velocity variation calculations and computational algorithms used were considerably

improved. The UU-P07 model is distinguished by a division of a single axial negative anomaly δVp into a chain of individual subvertical microplumes in the upper ~200 km (Fig. 1, item 1) in the research object. Outside the object, subvertical plume anomalies are at least 670 km deep. The given section does not show deeper mantle divisions under this boundary. Another feature of the mantle along the MAR near the object is cold blocks apparently typical of MAR segments with Hess crust type (Dmitriev et al., 2006). It should be noted that the SMS occurrences along the MAR in the research object are grouped above the "microplume" anomalies (Fig. 1, item 2) without deep roots. Under the slow spreading conditions with a low magma rate and shallow magma chambers, it can mean that SMSs are formed on certain basalt varieties (Silant'ev et al., 2023). It is possible that this interpretation is not the only one. The formation of negative δVp is also possible under the mantle serpentinization and decompression in the upper 25 km (Qin and Singh, 2015). In this case, decompressed blocks of this size (with a lower seismic wave velocity) will affect average values of the model parameterization cells with a larger size (100 km). In reality, both variants can occur.

The section (Fig. 1, item 1) shows two distinct minima corresponding to superimposed branches of the Iceland and Azores plumes. There are also signs of plumes with a lower intensity in the region of 10°, 35°,

and 50° S. Variations in seismic velocities control those in a mantle density and, accordingly, those in gravity field on the surface. Based on the comparison of the section with the data on free air gravity anomalies (Fig. 1, item 4) and Bouguer anomalies (Fig. 1, item 3), the low-frequency components of these fields, in terms of a position of extended anomalous zones, coincide with the seismotomographic section minima as decompressed mantle zones. The areas with a heated and decompressed material in Bouguer anomalies are observed as minima: they are deeper, when roots are deeper and amplitude δVp is higher in the anomalous mantle zones. Due to the fact that the magmatism productivity is particularly high in these zones, the terrain formed by basaltic eruptions has an increased value and is recorded as maxima in the free-air gravity field. Hence, geophysical characteristics shown along the MAR (Fig. 1, items 1, 2) at the level of extended (more than 500 km) anomalous zones of the section are characterized by antiphase trends and a consistent physically substantiated interpretation due to the rheological state of the mantle revealed by seismic tomography. Negative tomographic anomalies in the MAR northern segment are observed as branches from a deep channel and indicate the along-axis heated flow. The studied MAR segment containing SMS occurrences is located within the Bouguer anomaly maxima likely due to the most compact mantle areas under the ridge and a minimum magmatic flow. This region extends from ~7° S to ~25° N, and the maximum number of detected SMS occurrences are concentrated in its northern part.

The anomalous magnetic field (AMF) intensity in the MAR axial zone (Fig. 1, item 5) evidently depends on Fe content in basalts, because it forms the basic material of a magnetoactive layer. The relationship between the Fe content in different basalt varieties and the magnetization measured in samples is considered in (Verba et al., 2000). Statistical Fe contents in hardened basalt glasses in various plume and spreading assemblages are given in (Dmitriev et al., 2006). The correlation of the AMF, FeO, and basalt varieties along the MAR (Sokolov, 2016) is indicative of a similar distribution of the AMF (Maus et al., 2009) along the axial anomaly and the FeO content, especially in the northern plumes. Further south in the MAR zone, basalts are characterized by lower variations in FeO, and it was not possible to outline a sufficiently clear trend with the AMF. The MAR northern segment is characterized by an obvious relationship between the AMF amplitude, FeO content, and deep plume anomalies of the seismotomographic section (Fig. 1, item 1) in the Iceland and Azores plumes.

The described parameters were compared with other geophysical characteristics (Figs. 1, 2). The spatiotemporal seismicity structure along the MAR, constructed using the data from (ANSS, 2012; USGS, 2019) (Fig. 2, item 3), has all properties described by (Simao et al., 2010) for the MAR using the autonomous hydrophone data: it is an alternation of bands and voids which have shown zones with an increased and decreased seismicity since 1960. Single events are also present everywhere. Due to the fact that the teleseismic data accuracy is not high enough to tie the band to the framing of magmatic chambers, we consider a band position as related to the discrete magmatism source. Voids in the data with a high magnitude threshold (>4) are likely not representative of real weak seismicity. This should be taken into account when interpreting the magmatic origin of these bands and voids.

Primarily, the zones with the strongest and most stable seismicity over time are identified (Fig. 2, item 3). These zones correspond to the largest lateral displacements of the MAR axis along transform faults: Chain−Romanche−São Paulo group (from 1.5° S to 1.5° N), Arkhangelsky−Doldrums−Vernadsky group (from 7° to 9° N), Vema Fault (11° N), twin Charlie-Gibbs Fracture Zone (52° N), and a fragment of the Mohn Ridge adjacent to the Knipovich Ridge from the south (from 71° to 74° N) (Sokolov et al., 2020).

These zones are known for predominant strike-slip processes of sources (Boldyrev, 1998) and do not record the magmatic along-axis process, except for the eastern part of the Mohn Ridge (Fig. 2, item 3). Based on the seismic tomography section along the MAR (Fig. 2, item 1), these strike-slip zones are characterized by the shallowest position of the cold mantle, which causes increased fracturing between areas with contrasting properties. Another important feature of the spatiotemporal distribution (Fig. 2, item 3) is voids in seismicity. If we consider the most obvious cases—from 10° to 8° S (Fig. 2, items 3, 6, Ascension Island segment) and segments in the Azores and Iceland plumes (Fig. 2, item 1)—it becomes clear that these voids record high-productivity magmatism zones. According to the seismic tomography data (Fig. 2, item 1), voids almost everywhere correspond to the strongest negative anomalies indicating the low-viscosity zones within the axial negative velocity anomalies. The absence of teleseismic events with a high recording threshold in voids does not indicate the absence of seismicity in general. What is at issue is the absence of accumulation conditions for large stresses.

The key element of the spatiotemporal comparison of seismicity and δVp anomalies is a combination of local near-surface minima and bands which indicate the magmatic activity sources. The most expressive segment is that from the Cape Verde to Oceanographer faults, which borders the Azores plume to the south. It is a well-defined sequence of bands with a pseudoperiodicity of 1.5−2 arc degrees combined with local minima. This segment has a classical structure from the standpoint of the plate tectonics theory and was studied to substantiate the latter. In addition, it is the most ancient MAR segment (170 Ma) (Müller et al., 2008) and contains a cold region in the upper
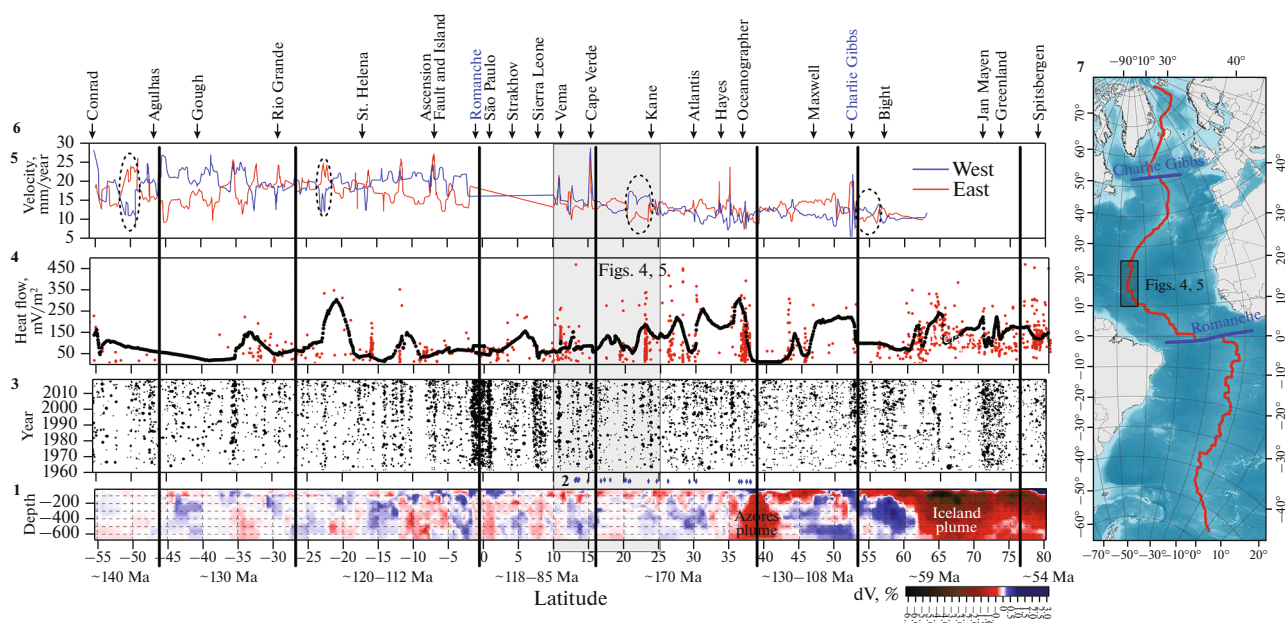
Fig. 2. Correlation of geological and geophysical parameters along MAR axis after (Sokolov, 2018 with modifications) and MAR segmentation depending on age of initiated spreading processes after (Sokolov et al., 2020). Study area is indicated with gray rectangle. (1) Variations in velocities δVp according to UU-P07 model (Amaru, 2007; Hall and Spakman, 2015; Van der Meer et al., 2018); (2) locations of SMS deposits after (Beaulieu and Szafranski, 2020) and data obtained by VNIIOkeangeologia in study area; (3) spatiotemporal correlation of seismic events after (ANSS, 2012; USGS, 2019) since 1960, a symbol size is graded in terms of magnitude, and events are shown in horizontal projection on latitude axis; (4) heat flow values after (Podgornykh and Khutorskoi, 1997; Global..., 2018) (red dots) and cross-section of grid calculated from these data by kriging method in MAR profile (black dots); (5) spreading half-rates (mm/year) along 4 Ma isochron, shown by a pair for MAR western and eastern flanks, plotted from (Müller et al., 2008) with a blanked interval from 2° S to 10° N due to low reliability of values obtained; ellipses encircle inverse regions with a noticeable predominance of eastern spreading half-rates in Southern Hemisphere and western half-rates in Northern Hemisphere; (6) intersection with MAR and names of major transform faults; (7) map of Atlantic region with MAR position in profile (red line); Romanche and Charlie Gibbs demarcation faults (blue lines) and SMS-rich area (black rectangle) whose geological and geophysical parameters are given in Figs. 4 and 5.

mantle near axial microplumes (Fig. 2, item 1). In the North Atlantic region, a similar overprinting of plume magmatism on the MAR is well-defined and begins from the southern framing of the Azores plume and further north in the area where the Iceland plume passes into the MAR axis. Taking into account the data (Dmitriev et al., 2006) on the basalt distribution in two main assemblages such as plume and spreading, most samples with spreading basalts TOR-2 (N-MORB) are distributed in the indicated segments of the South and North Atlantic regions. Samples dominated by the plume assemblage TOR-1 (E-MORB) are located mostly in the areas which (on the maps of teleseismic events) contain voids above plume outflows with the increased-productivity magmatism.

Heat flow (HF) is a parameter which records the geodynamic status of the subsurface and its thermal nonequilibrium degree (Fig. 2, item 4). For this reason, it is expedient to compare HF with the tomography data along the active divergent MAR boundary and with age. For this, we used the data from the global heat flow databases (Podgornykh and Khutorskoi, 1997; Global..., 2018) obtained in the MAR zone (Fig. 2, item 4, red dots), in a 200 km band. According

to these data, anomalously high, "zero," and even negative values of conductive HF density were obtained in rift basins along the MAR. Since the ocean floor spreading is accompanied by the mantle material intrusion, the observed HF is formed not only by conductive but also by convective heat transfer under volcanism processes and by hydrothermal circulation systems developed in the rift basins. We did not take into account high HF values obtained in the discharge areas of hydrothermal systems. Most of these values are greater than 1 W/m² and do not adequately record the heat loss due to the heat conduction. Extreme HF values recording the conductive heat transfer through loose bottom sediments reach a few hundreds of mW/m² in the MAR band within the fifth identified magnetic anomaly.

To analyze the HF in a continuous mode along the MAR, the unevenly distributed cloud of measurement points was interpolated onto a grid with a uniform step of 1 arc degree. A section was made on this grid using the MAR profile (Fig. 2, item 4, black line). Based on the comparison with the thermal state of the mantle according to the tomography data (Fig. 2, item 1), the HF distribution along the axial zone is complex

mosaic, but the general trend toward increasing values above mantle plume branches is obvious. Because the MAR was segmented by the age of the initiated spreading processes and a trend toward a decrease in the thermal state with age is observed at a qualitative level (Fig. 2, item 1), the evolution of this condition along the MAR can be studied by comparing the tomography data with average HF values within non-coeval segments (Sokolov et al., 2020). The most ancient segment with a spreading onset age of ~170 Ma is characterized by low average HF values in its southern part in the SMS-rich region, without taking into account huge convective values measured directly within hydrothermal vent sites.

A spreading rate is the most important parameter of the course of geodynamic processes based on mantle heterogeneities. Spreading half-rates along the 4 Ma isochron, shown in pairs for the western and eastern flanks of the MAR and constructed according to data from (Müller et al., 2008), are given in the interval from 1° S to 10° N (Fig. 2, item 5). This approach is used, because the equatorial segment contains a highly fragmented anomalous magnetic field, no reliable linear anomalies are distinguished in this interval, and errors in calculating the half-rates too high. The spreading rate gradually increases with some distance from the pole of rotated plates separated by the MAR (about 60° N). Local variations in half-rates are observed on this background: they reach 100% along the strike of the MAR and up to 250% in the difference between its western and eastern flanks.

Based on spreading rates obtained along the MAR and its flanks along noncoeval isochrons (Mashchenkov et al., 1992), they are subjected to discrepancies (by more than two times) in the kinematics of adjacent spreading segments separated by transform faults. Under these conditions, horizontally differentiated displacements and strike-slips will occur within the plates orthogonal to the MAR not only in active fault areas, but also in passive ones, far from the rift zone, due to an additional strike-slip component acquired from the difference in rates. In addition, the indicated difference in rates may apparently be due to axis jumps. Asymmetry is also observed in the western and eastern flanks in the velocity distribution generally estimated from values on one side of the MAR and called half-rates (Fig. 2, item 5). The asymmetry is reduced to almost zero in some MAR segments.

The half-rates of the MAR western flank in the Southern Hemisphere are higher than on the eastern flank; vice versa, in the Northern Hemisphere, half-rates of the eastern flank prevail over those of the western (Fig. 2, item 5). Taking into account the common western component of plate drift (Tveritinova, 2010), the fixed position of the African Plate with respect to deep magmatism sources in the Atlantic region (Mazarovich, 2000), and the general sublatitudinal displacement of the North American Plate to the west

according to (GPS, 2008), the prevalence of eastern MAR half-rates in the Northern Hemisphere can be explained under the current observations of horizontal plate movement vectors (Sokolov et al., 2022). It should be noted that the opposite effect of the general asymmetry of spreading half-rates along the MAR in the northern and Southern Hemispheres is indicative of the influence of the Earth's rotation effects on the geodynamics of the described processes, and, possibly, the Coriolis force, but the study of this influence is beyond the scope of this work.

Based on the half-rates profiles compared in the 4 Ma isochron (Fig. 2, item 5), the largely western (or eastern) dominance of half-rates in the corresponding hemisphere undergoes a local inversion in some segments. These spatial inversions occur in both hemispheres at approximately the same latitudes: between 20° and 25°, and also around 50° and 55°. These values are located toward the poles and toward the equator from the critical latitude of 35°16′ which is important for the geometry of tectonic processes on a rotating spheroid (Lichkov, 1965).

The inversion within 20° and 24° N is closely south of the Kane Fracture Zone (Fig. 2, items 5, 6). Being determined from the 4 Ma isochron (~120 km from the MAR axis), it is indicative of the fact that this segment is unstable, and a spreading axis jump is highly probable, capable of resulting in an apparent change and difference in the spreading rate. Within 50 km from the MAR geometric axis (Fig. 3), the active axis continued (according to the current seismicity data) in this segment, to the west of the position that would be reasonably traced solely based on the terrain data. This MAR segment was also identified from several south-oriented nontransform displacements. All of the aforesaid is indicative of local instability in the mantle recorded in variations of trends in thin lithospheric blocks segmented by transform faults.

CORRELATION OF DETAILED GEOPHYSICAL DATA ALONG THE NORTHERN SUBEQUATORIAL SEGMENT OF THE MAR

To analyze the geophysical data along the northern equatorial segment of the MAR, a fragment of the seismic tomographic section along the MAR was taken according to the UU-P07 model (Amaru, 2007; Hall and Spakman, 2015; Van der Meer et al., 2018) from the Vema Fracture Zone to the Kane Fracture Zones (Fig. 4, item 1). The SMS deposits are concentrated above areas with negative δVp down to a depth of ~200 km. When the model with a spatial resolution of 50−100 km is used, all density inhomogeneities within this size are included in the parameterization cell and averaged. In other words, negative δVp regions can contain, in undivided form, both local micro-plumes with heated and partially molten mantle and zones with a decompressed mantle related to ser-
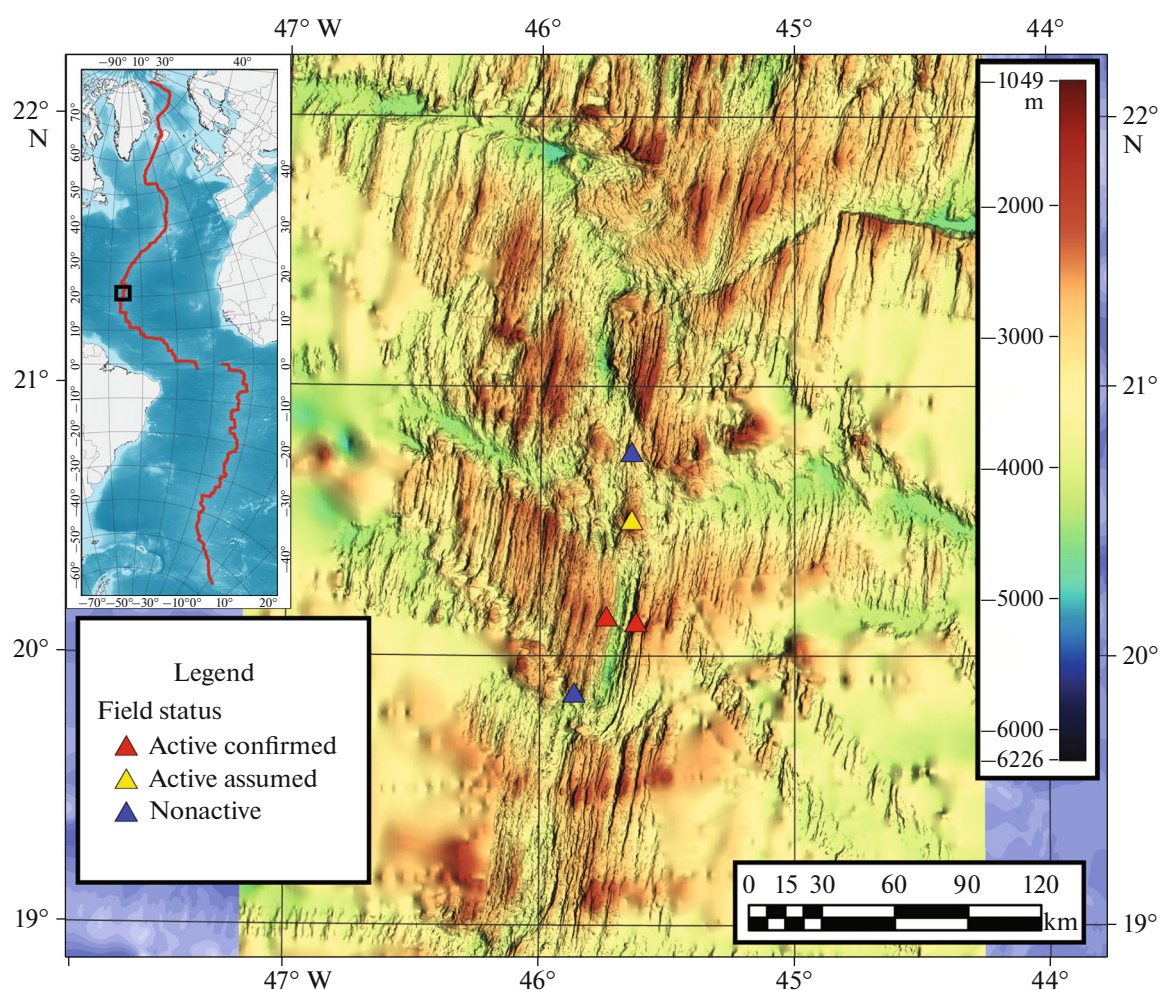
Fig. 3. Multibeam bathymetry configuration based on data obtained by VNIIOkeangeologia (https://www.вниио.рф/en/) and Lamont Doherty Earth Observatory (https://www.ldeo.columbia.edu/research/databases-repositories) in area of detected SMS deposites from 19 to 22° N after (Beaulieu and Szafranski, 2020). Inset shows a position of map on MAR axis.

pentinization. It is not possible to distinguish these effects using seismic tomography data. Cold lenses were also found in the upper mantle, within the SMS occurences (~13.5°, 15.3°, and 23.5° N).

To obtain more details on the upper part of the mantle section, Bouguer anomalies were calculated with the use of a detailed 1′ grid (Sandwell and Smith, 2009) with the following density values: water 1.03 g/cm^3, crust 2.80 g/cm^3, and mantle 3.25 g/cm^3, because the analysis area was located in the MAR axial part. The terrain data were taken from the 100-meter grid of multibeam bathymetry of the VNIIOkeangeologia (https://www.вниио.рф/en/) and Lamont Doherty Earth Observatory (https://www.ldeo.columbia.edu/research/databases-repositories) averaged onto a 1′ grid for compatibility with free air anomalies and to avoid artifacts of projection of detailed terrain into density inhomogeneities unidentifiable with the same detail in terms of gravity field.

Bouguer anomalies and the terrain along the MAR axis (Fig. 4, items 3, 4) are distinguished by a negative correlation along the entire length of the studied MAR segment, except for the area with V-shaped nontransform displacements (Fig. 3). The anticorrelation is related to the fact that the areas with local minima of Bouguer anomalies, interpreted as the effect of a heated or partially molten mantle, are characterized by more productive magmatism which forms a hypsometrically more elevated terrain on the surface. This relationship is maintained almost throughout the entire northern equatorial segment of the MAR. However, there is an exception in this region: within its boundaries, the correlation between the terrain and Bouguer anomalies is direct. The path of the MAR axis was drawn along the areas with a well-defined rift valley, and in complex cases, where the terrain geometry does not provide an unambiguous idea of the axis position (Fig. 3), along the area of current seismicity. It should be noted that in most of the northern equa-
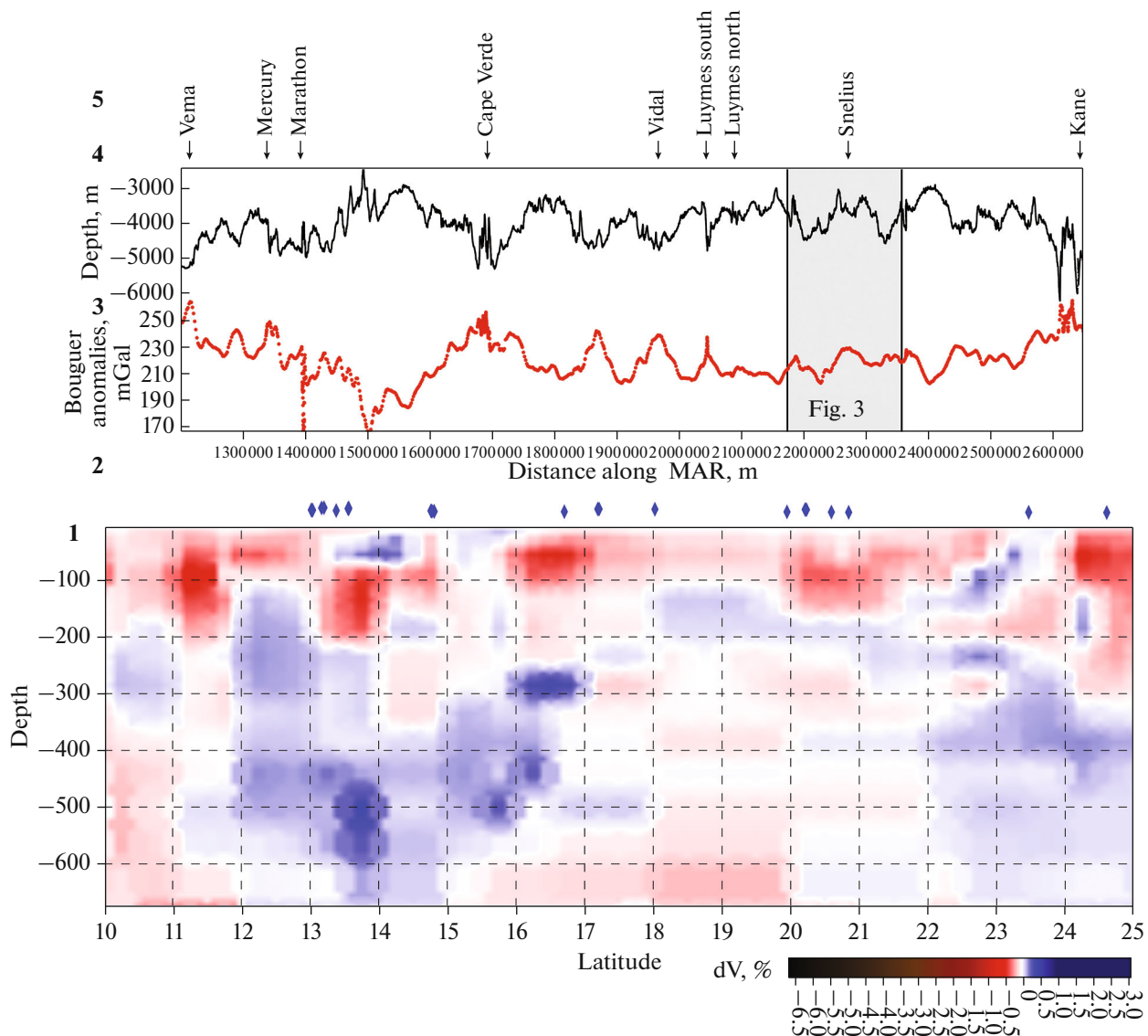
Fig. 4. Correlation of detailed geological and geophysical parameters along SMS survey area between Vema and Kane fracture zones. Gray rectangle shows SMS study area (Fig. 3) with pronounced nontransform displacements. (1) Variations in velocities δVp according to UU-P07 model (Amaru, 2007; Hall and Spakman, 2015; Van der Meer et al., 2018); (2) Location of detected SMS deposits according to data obtained by (Beaulieu and Szafranski, 2020) and VNIIOkeangeologia in study area; (3) Bouguer anomalies (mGal) on 1′ grid; (4) bottom terrain along MAR axis averaged to 1′ grid; (5) intersection with MAR and names of major transform faults.

torial segment of the MAR, a position of the seismic event cloud coincides with the rift valley, well-defined in the terrain. The seismicity deviation to the west from the spreading geometric focus is observed within the region with V-shaped nontransform displacements (Fig. 3).

The two options for interpreting this combination of parameters of the anomalous field and the terrain have different meaning.

The study area (Fig. 3) is located above the nonserpentinized outcrop of ultramafic rocks with a density of ~3.25 g/cm^3 (or more); this value is ~15% greater than a density of basalts, and this difference in value is about several tens of mGal in the gravity field from different MAR segments (Fig. 4, item 3); this value is well-defined in the satellite altimetry data obtained with an accuracy of 1.5−2.0 mGal. The Cape Verde Fault Zone provided a lot of ultramafic rocks (Silant'ev et al., 2023), as well as the rift segments of the (Fig. 3) MAR region, is characterized by a direct correlation of Bouguer anomalies and the terrain, as well as by a strong contrast with the more southern region, where a plume can be seen in the seismic tomography section (Fig. 4, item 1). Based on the direct correlation along the fault zones with confirmed ultramafic rocks, the meaning of this interpretation option lies in the presence of ultramafic rocks along
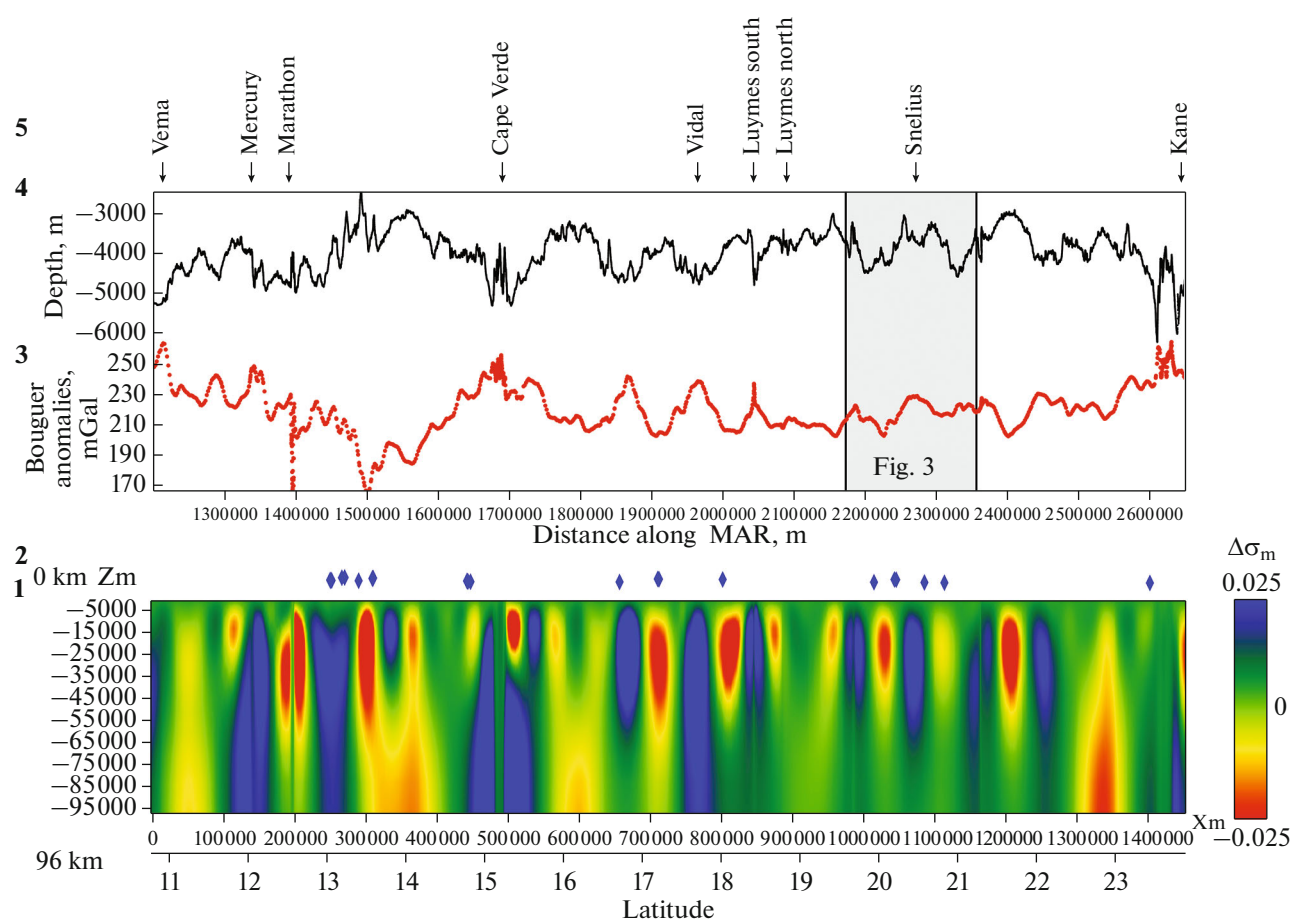
Fig. 5. Correlation of detailed geological and geophysical parameters along SMS survey area between Vema and Kane fracture zones. Gray rectangle shows the SMS study area (Fig. 3) with pronounced nontransform displacements. (1) Relative density variations calculated using density inversion procedure of ZondGM2D software package (Kaminsky, 2017), density values are conditional; (2) Location of detected SMS deposits according to data obtained by (Beaulieu and Szafranski, 2020) and VNIIOkeangeologia in study area; (3) Bouguer anomalies (mGal) on 1′ grid; (4) bottom terrain along MAR axis averaged to 1′ grid; (5) intersection with MAR and names of major transform faults.

the MAR region (Fig. 3), possibly accompanied by vertical movements with a positive sign as an asymmetric isostatic compensation of one of the rift walls during extension.

Another option for interpreting the direct correlation in the area shown in Fig. 3 is the following. Since a clear westward shift of the extension axis is observed in the region from 20.5° to 21.5° N, also recorded in the current seismic events, it can be suggested that the ongoing jump of the MAR axis in this segment is accompanied by the initiated magmatism, not yet sufficient to form a negative variation of the Bouguer anomaly. This jump is also accompanied by the formation of a relatively deepened rift segment around 21° N. This explains the direct correlation between terrain graph minima and Bouguer anomalies in the region shown in Fig. 3. In this case, basalts should contain markers indicating re-melting of the previously depleted mantle (Sanfilippo et al., 2021) after the jump. The direct correlation of the maxima of

these parameters can be explained by the fact that the area shown in Fig. 3 is already characterized by intensive melting accompanied by terrain uplifting or melting processes in the MAR flank more elevated than the valley, but still devoid of extensive mantle sources of heated material. This interpretation option explains the direct correlation of parameters without the widespread occurrence of ultramafic rocks. According to (Silant'ev et al., 2023), mainly basalts were sampled along this MAR segment, and SMS deposits identified in this area hosted by basalts.

Hence, the most probable interpretation, in our opinion, is the westward movement of the active rift system, rather than the occurrence of ultramafic rocks in the MAR axis.

Based on the comparison of the parameter graphs along the MAR axis, similar to Fig. 4, with the density inversion results obtained using ZondGM2D software (Kaminskii, 2017) without additional correction (Fig. 5), the area of positive correlation of Bouguer

anomalies and the terrain (Fig. 3) between Vema and Kane fracture zones is represented by negative density anomalies with the lowest amplitude along the studied area. To the south of it, up to 18.5° N, small negative density anomalies are also observed, but the correlation with terrain remains negative. The most striking density anomaly is observed in the segment from 13.5° to 14.5° N. It is even possible to trace the southward displacement of the heated region as it rises from depth. In this segment, a similar result can be seen in the seismic tomography pattern from a depth of 200 km (Fig. 4, item 1).

CONCLUSIONS

The section of the UU-P07 seismic tomographic model demonstrates a disintegration of a uniform axial negative anomaly δVp into a chain of individual subvertical microplumes in the upper ~200 km between Vema and Kane fracture zones. Cold blocks are observed deeper, typical of the MAR segments with Hess crust type. Positions of SMS deposits along the MAR in the research object are grouped above microplume-type anomalies without deep roots. In slow spreading conditions, at a low magma flow rate with shallow chambers, this can mean that the SMS deposits are related to a certain basalt type. Negative δVp can also form during serpentinization and decompaction in the upper mantle. Decompressed blocks with a lower seismic wave velocity will affect the average values of the model parameterization cells with a size of ~100 km. In reality, both options can be implemented.

At a scale level of 500 km or more, free air and Bouguer anomalies are characterized by antiphase trends and a consistent, physically justified interpretation due to the rheological status of the mantle revealed by the seismic tomography. Negative tomographic anomalies in the MAR northern segment are configured as branches from a deep channel and indicate an along-axis heated flow. The MAR segment from Vema to Kane fracture zones is located in the region of maximum Bouguer anomaly values likely due to the most compact mantle areas under the ridge and a minimum magmatic flow. This area extends from ~7° S to ~25° N, and the largest number of SMS deposits were found in its northern part. The northern segment of the MAR is distinguished by an obvious relationship between the AMF amplitude and deep plume anomalies of the seismotomographic section in the Iceland and Azores plumes.

The spatiotemporal seismicity structure along the MAR, according to the teleseismic data, with a magnitude of at least 4 has well-defined features such as bands and voids. Based on the interpretation of seismicity bands in combination with δVp minima, the seismicity is explained by discrete laterally heated and partially molten mantle zones where the ascent of material results in an anomalous δVp field and stable shaking. Major band manifestations correspond to the MAR segments dominated by the low-temperature and shallow-depth spreading magmatism. Seismicity voids are interpreted from the standpoint of highly productive plume magmatism characterized by a low-viscosity mantle, no accumulation of high stresses, and frequent and weak seismic events being within the detection threshold. Wide bands of intensive seismicity correspond to fault zones with strike-slip events subjected to large lateral displacement of the MAR axis. The MAR segment located between the Vema and Kane fracture zones is characterized by the most pronounced alternation of voids and seismicity bands with a step of ~1.5°, which is comparable with the framing of near-surface δVp minima and the areas with grouped SMS deposits.

Comparisons of the heat flow with the age of initiated spreading processes and seismic tomography values δVp obtained for MAR segments confirm that the generally accepted thermal interpretation of seismic tomography data is correct. The northern near-equatorial segment of the MAR between Vema and Kane fracture zones, after huge heat flow values are excluded from the analysis, is characterized by a low average conductivity value compared to the segments with plume outflows.

The inversion of prevailing spreading rates from the MAR eastern flank to the western flank within 20° and 24° N is observed immediately south of the Kane Fracture Zone. Within 50 km from the MAR geometric axis in this segment, according to the current seismicity data, an active axis continued to the west of the geometric position, according to the terrain data. This MAR segment is also identified from south-oriented nontransform displacements. This fact is indicative of local mantle instability recorded in trend variations of thin lithosphere blocks segmented by transform faults.

When using the seismic tomographic model with a spatial resolution of 50−100 km, all density inhomogeneities within this size are included in the parameterization cell and averaged. In other words, negative δVp regions can contain, in undivided form, both the local microplumes with a heated and partially molten mantle and the zones with a decompressed mantle related to serpentinization. It is not possible to distinguish these effects based on the seismic tomography data.

A main feature used to compare Bouguer anomalies and the terrain is a negative correlation throughout the entire northern equatorial segment of the MAR, except for the region from 19° to 22° N, where V-shaped nontransform displacements are evident. The areas with local minima of Bouguer anomalies, interpreted as the effect of a heated or partially molten mantle, are characterized by a more productive magmatism resulting in a hypsometrically more elevated terrain on the surface.

In the region from 19° to 22° N, the correlation between terrain and Bouguer anomalies is positive.

The MAR axis path in this region was drawn along the current seismicity area. The seismicity deviation to the west from the spreading geometric focus is observed within the region with V-shaped nontransform displacements.

The first interpretation option of the positive correlation suggests ultramafic rocks along the region from 19° to 22° N and possible vertical movements with a positive sign as an asymmetric isostatic compensation of one of the rift walls under extension in a new location.

Another interpretation option of the direct correlation is based on the currently occurring jump of the MAR axis in this segment and the initiated magmatism not yet sufficient to form a negative variation of Bouguer anomaly. The direct correlation of the maxima of these parameters can be explained by intensive melting with uplifts or melting processes on the flank of the MAR more elevated than the valley, but still not having extensive mantle sources of heated material. This interpretation option considered as the most likely is related to the active rift system switching to the west, rather than to the ultramafic rock occurrence on the MAR axis. The comparison of these data with the density inversion results also confirms this option.

FUNDING

CONFLICT OF INTEREST

The authors of this work declare that they have no conflicts of interest.

REFERENCES

M. Amaru, "Global travel time tomography with 3-D reference models," Geologica Ultraiectina **274** (2007).

ANSS Earthquake Composite Catalog (Historical) (2012). https://ncedc.org/anss/catalog-search.html. Access date: December 31, 2012.

S. E. Beaulieu and K. Szafranski, InterRidge Global Database of Active Submarine Hydrothermal Vent Fields, Version 3.4. (2020). World Wide Web electronic publication available from http://vents-data.interridge.org. Accessed January 17, 2023.

T. W. Becker and L. Boschi, "A comparison of tomographic and geodynamic mantle models," Geochem., Geophys., Geosyst. **3**, 1−48 (2002). https://doi.org/10.129/2001GC000168

S. A. Boldyrev, *The Seismic Geodynamics of the Mid-Atlantic Ridge* (NGK RF, Moscow, 1998).

E. Bonatti, "Origin of the large fracture zones offsetting the Mid-Atlantic Ridge," Geotectonics **30** (6), 430−440 (1996).

L. V. Dmitriev, S. Yu. Sokolov, and A. A. Plechova, "Statistical assessment of variations in the compositional and P−T parameters of the evolution of mid-oceanic ridge basalts and their regional distribution," Petrology **14** (3) 209−229 (2006).

Global Heat Flow Database (University of North Dakota, 2018). https://engineering.und.edu/research/global-heat-flow-database/data.html.

GPS Time Series Data (Jet Propulsion Laboratory of California Institute of Technology, 2008. http://sideshow.jpl.nasa.gov/mbh/series.html.

R. Hall and W. Spakman, "Mantle structure and tectonic history of SE Asia," Tectonophysics **658**, 14−45 (2015).

A. E. Kaminsky, Software Package ZOND (2017). http://zond-geo.ru.

B. L. Lichkov, *To the Basis of Modern Earth Theory* (LSU Publishers, Leningrad, 1965).

S. P. Mashenkov, E. M. Litvinov, A. G. Gorshkov, and I. P. Lukashevich, "Geophysical criteria for identifying regional environments favorable for the formation of deep-sea polymetallic sulfides," *Deep Structure and Geodynamics of the Lithosphere of the Atlantic and Pacific Oceans*, Ed. by I. S. Gramberg and P. A. Stroev (Nauka, Moscow, 1992), pp. 151−178.

S. Maus, U. Barckhausen, H. Berkenbosch, et al., "EMAG2: A 2-arc-minute resolution Earth Magnetic Anomaly Grid compiled from satellite, airborne and marine magnetic measurements," Geochem., Geophys., Geosyst. G3 **10** (8), 1−12. https://doi.org/10.1029/2009GC002471

A. O. Mazarovich, *Geology of the Central Atlantic: Fractures, Volcanic Edifices and Oceanic Bottom Deformations* (Nauchyy Mir, Moscow, 2000).

R. D. Müller, M. Sdrolias, C. Gaina, and W. R. Roest, "Age, spreading rates, and spreading asymmetry of the world's ocean crust," Geochem., Geophys., Geosyst. G3 **9** (4), 1−19 (2008). https://doi.org/10.1029/2007GC001743

L. V. Podgornykh and M. D. Khutorskoy, *Heat Flow Planetary Map 1 : 30000000. Explanatory Note* (Moscow−St.-Petersburg, 1997).

Y. Qin and S. C. Singh, "Seismic evidence of a two-layer lithospheric deformation in the Indian Ocean," Nat. Commun. **6**, 8298 (2015). https://doi.org/10.1038/ncomms9298

D. T. Sandwell and W. H. F. Smith, "Marine gravity anomaly from Geosat and ERS-1 satellite altimetry," J. Geophys. Res. **102** (B5), 10039−10054 (1997). ftp://topex.ucsd.edu/pub/.

D. T. Sandwell and W. H. F. Smith, "Global marine gravity from retracked Geosat and ERS-1 altimetry: Ridge segmentation versus spreading rate," J. Geophys. Res.: Solid Earth **114** (B1), 1−18 (2009). https://doi.org/10.1029/2008JB006008

A. V. Sanfilippo, J. M. Salters, S. Yu. Sokolov, A. A. Peyve, and A. Stracke, "Ancient refractory asthenosphere revealed by mantle re-melting at the Arctic Mid Atlantic Ridge," Earth Planet. Sci. Lett. **566** (116981), 1−10 (2021).

S. A. Silantyev, A. I. Buikin, A. R. Tshovrebova, et al., "Variations in the composition of MORB chilled glasses from the Mid-Atlantic Ridge, 12°−31° N: reflection of compositional evolution of parental melts and the influence of a hydrothermal component," Petrology **31** (5), 1−19 (2023).

N. Simao, J. Escartin, J. Goslin, et al. "Regional seismicity of the Mid-Atlantic Ridge: observations from autonomous hydrophone arrays," Geophys. J. Int. **183**, 1559−1578 (2010).
https://doi.org/10.1111/j.1365-246X.2010.04815.x

S. Yu. Sokolov, "Tectonic peculiarities of the Mid-Atlantic Ridge based on data on correlation between surface parameters and geodynamic state of the upper mantle," Vestn. KRAUNTs. Nauki o Zemle No. 4 (32), 88−105 (2016).

S. Yu. Sokolov, *Tectonics and Geodynamics of the Atlantic Equatorial Segment* (Mauchn. Mir, Moscow, 2018).

S. Yu. Sokolov, N. P. Chamov, M. D. Khutorskoy, and S. A. Silantyev, "Intensity indicators of geodynamic processes along the Atlantic-Arctic rift system," Geodynam. Tectonophys **11** (2), 302−319 (2020).
https://doi.org/10.5800/GT-2020-11-2-0476

S. Yu. Sokolov, K. O. Dobrolyubova, and N. N. Turko, "Relationships of surface geological and geophysical characteristics with the deep structure of the Mid-Atlantic Ridge according to seismic tomography data," Geotectonics **56** (2), 107−122 (2022).
https://doi.org/10.31857/S0016853X22020060

W. J. Su and A. M. Dziewonski, "Simultaneous inversion for 3-D variations in shear and bulk velocity in the mantle," Phys. Earth Planet. Inter. **100** (1−4), 135−156 (1997).

T. Yu. Tveritinova, "Wave tectonics of the earth," Geodynam. Tectonophys. **1** (3), 297−312 (2010).
https://doi.org/10.5800/GT-2010-1-3-0023

USGS Earthquake Composite Catalog. 2019. https://earthquake.usgs.gov/earthquakes/search/. Query February 16, 2019.

D. G. Van der Meer, D. J. Van Hinsbergen, and W. Spakman, "Atlas of the underworld: Slab remnants in the mantle, their sinking history, and a new outlook on lower mantle viscosity," Tectonophysics **723**, 309−448 (2018).

V. V. Verba, G. P. Avetisov, T. V. Stepanova, and L. Y. Sholpo, "Basalts geodynamics and magnetism of the Knipovich underwater ridge Norway-Greenland basin," Russ. J. Earth Sci., No. 4, 303−312 (2000).

Y.S. Zhang and T. Tanimoto, "Ridges, hotspots and their interaction, as observed in seismic velocity maps," Nature **355** (6355), 45−49 (1992).

Translated by E. Maslennikova